

Numerical analysis of heating rate effect on spalling of high-performance concrete under high temperature conditions

Zhao, Jie; Zheng, Jian Jun; Peng, Gai Fei; van Breugel, Klaas

DOI

[10.1016/j.conbuildmat.2017.07.023](https://doi.org/10.1016/j.conbuildmat.2017.07.023)

Publication date

2017

Document Version

Accepted author manuscript

Published in

Construction and Building Materials

Citation (APA)

Zhao, J., Zheng, J. J., Peng, G. F., & van Breugel, K. (2017). Numerical analysis of heating rate effect on spalling of high-performance concrete under high temperature conditions. *Construction and Building Materials*, 152, 456-466. <https://doi.org/10.1016/j.conbuildmat.2017.07.023>

Important note

To cite this publication, please use the final published version (if applicable). Please check the document version above.

Copyright

Other than for strictly personal use, it is not permitted to download, forward or distribute the text or part of it, without the consent of the author(s) and/or copyright holder(s), unless the work is under an open content license such as Creative Commons.

Takedown policy

Please contact us and provide details if you believe this document breaches copyrights. We will remove access to the work immediately and investigate your claim.

1 **Numerical analysis of heating rate effect on spalling of high-performance concrete**
2 **under high temperature conditions**

3

4 Jie Zhao ^{a,*}, Jian-Jun Zheng ^b, Gai-Fei Peng ^a, Klaas van Breugel ^c

5

6 ^a School of Civil Engineering, Beijing Jiaotong University, Beijing 100044, P. R. China.

7 ^b School of Civil Engineering and Architecture, Zhejiang University of Technology,

8 Hangzhou 310014, P. R. China.

9 ^c Faculty of Civil Engineering and Geosciences, Delft University of Technology, 2628 CN

10 Delft, the Netherlands.

11

12 **ABSTRACT**

13 High-performance concrete (HPC) is vulnerable to spalling under high temperature
14 conditions and it has been found that the heating rate can exert a tremendous effect on
15 spalling of HPC. To prevent HPC from spalling, the heating rate effect should be understood.
16 However, quantitative analyses are still lacking and the heating rate effect has not been well
17 interpreted so far. In this paper, a numerical analysis of the heating rate effect on spalling of
18 HPC is presented. Based on the experimental results reported in the literature, the spalling
19 behavior of cubic HPC specimens under fire heating and slow heating with a heating rate of 5
20 °C/min is modeled. With a meso-level thermo-chemo-hydro-mechanical analysis, the
21 temperature gradient induced thermal stress and the mechanical effect of build-up vapor
22 pressure are investigated. The results show that, at different heating rates, the spalling
23 mechanisms are different. Finally, possible manners and mechanisms of spalling are
24 discussed.

25

26 **Keywords:** High-performance concrete; High temperature; Heating rate; Spalling

27

28 _____

29 *

30 E-mail address: zhaojie@bjtu.edu.cn (J. Zhao).

31

32

33 **1. Introduction**

34 Nowadays, high-performance concrete (HPC) has been widely used in various structures
35 due to its high strength and excellent durability. However, under high temperature conditions,
36 such as fire, HPC is vulnerable to spalling, which greatly endangers the safety of HPC
37 structures. How to prevent HPC from spalling has become a great concern in the fire safety
38 design of HPC structures. To investigate spalling of HPC, many experimental investigations
39 have been conducted and it has been found that the heating rate can exert a tremendous effect
40 on spalling of HPC.

41 Hertz [1] and Anderberg [2] concluded that the risk of explosive spalling of dense
42 concrete increased with the increase in the heating rate. Phan and Carino [3] observed that,
43 under slow heating with a heating rate of 5 °C/min, cylinder specimens of high strength
44 concrete spalled when the surface temperature was in the range of 280 °C to 320 °C after
45 heating for about two hours. Peng [4] found that spalling of HPC occurred at the heating time
46 of about 170 second under the ISO 834 standard fire, while Yan et al. [5] found that spalling
47 occurred much early at the heating time range of 30 to 120 seconds under hydrocarbon fire.
48 Peng [4] also found that HPC did not spall under slow heating conditions. Yan et al. [6]
49 reported that the spalling mode of 150 mm cubic high strength concrete specimens was
50 heating rate dependent, i.e. under slow heating with a heating rate of 2 °C/min, specimens
51 spalled into small pieces, while under the BS 476 standard fire condition, only the corners of
52 specimens spalled. Kanéma et al. [7] applied two heating rates to concrete specimens and
53 found that $\Phi 0.16 \times 0.32$ m cylindrical high strength concrete specimens spalled when the
54 heating rate was 1.0 °C/min, but did not spall when the heating rate was 0.1 °C/min. Klingsch
55 et al. [8] experimentally investigated the effect of the heating rate in the range of 0.25 to 8.0
56 K/min on spalling of HPC cylinders ($\Phi 0.15 \times 0.30$ m). Two different types of spalling were
57 observed, that is, spalling started from the surface layer at high heating rates and initiated from

58 the core at low heating rates. It was also found that spalling can be avoided by decreasing the
59 heating rate or the strength of concrete.

60 From the above experimental investigations it can be seen that the heating rate can exert
61 effects not only on the spalling occurrence but also on the spalling manner of HPC. In addition to
62 the experimental investigations, a number of numerical modeling contributions have been
63 made by researchers to explain and to assess the spalling risk of concrete. Ulm et al. [9,10]
64 developed a chemo-plastic model to analyze the fire-induced spalling of concrete rings of the
65 Channel Tunnel. Ichikawa and England [11], Dwaikat and Kodur [12], and Beneš and Štefan
66 [13] proposed one-dimensional models to simulate the spalling of concrete elements. Tenchev
67 and Purnell [14] studied the fire spalling of a concrete wall on an arithmetic parallel averaged
68 meso-level. Gawin et al. [15] used a fully coupled model and employed four spalling indices
69 of different failure modes for the concrete spalling analysis. De Morais et al. [16] numerically
70 analyzed spalling of a cylindrical specimen subject to slow heating with a heating rate of 1
71 °C/min at a macro level. Fu and Li [17] simulated the progressive spalling of concrete
72 subjected to a constant temperature of 1200 °C by analyzing the thermal stress-induced
73 damage. Zhang and Davie [18] analyzed fire spalling of a concrete wall and a concrete
74 column. By developing Gawin's model, Zhang et al. [19] estimated the fire spalling risk of
75 concrete by comparing the strength profile with the stress profile in concrete. Xotta et al. [20]
76 investigated the effects of the porosities of aggregate and cement paste on the internal stresses
77 of heated concrete under slow and fast heating conditions at a meso-level. Based on the
78 experiments and by analyzing the thermal stress development, Ju et al. [21] modeled the
79 spalling process of reactive powder concrete specimens exposed to slow heating with a
80 heating rate of 4.8 °C/min.

81 From the above existing modeling work of spalling it can be seen that the investigation
82 of the heating rate effect on spalling is still insufficient. To prevent HPC from spalling, the

83 heating rate effect on spalling should be well understood. Although, two hypotheses have
84 been proposed to explain spalling: the vapor pressure mechanism [3,4,22,23] and the
85 temperature gradient-induced thermal stress mechanism [9,10,24,25], the heating rate effect
86 on the spalling mechanism of HPC still needs to be clarified and the quantitative analyses of
87 the heating rate effect are still lacking. Thus, the purpose of this paper is to investigate the
88 heating rate effect on spalling of HPC. To this end, HPC cubes with a side length of 100 mm
89 under two heating conditions, i.e. the ISO 834 standard fire and slow heating with a heating
90 rate of 5 °C/min, reported in Peng's experiments [4] are numerically modeled at a meso-level.
91 With a thermo-chemo-hydro-mechanical analysis, the temperature field, the moisture
92 transport, the vapor pressure build-up, and the internal stress induced by the temperature
93 gradient and vapor pressure are modeled. The effects of the temperature gradient and vapor
94 pressure on spalling of the specimens under the two heating conditions are analyzed. The
95 heating rate effect on spalling of HPC is then quantitatively interpreted.

96

97 **2. Model description**

98 To model the heating rate effect on spalling of HPC, the complex chemical and physical
99 reactions of concrete to high temperatures are modeled at a meso-level and briefly presented
100 as follows.

101 **2.1 Thermal decomposition based material properties of cement paste**

102 When exposed to elevated temperatures, cement paste will undergo decomposition,
103 resulting in the variation of various constituents and hence the variation of material properties.
104 Zhao et al. [26] proposed a thermal decomposition prediction model. In the model, by
105 considering the kinetics of thermal decomposition, the conversion degree of each hydration
106 product in cement paste is determined as a function of heating history. Thus, with the initial
107 volume fractions of various constituents f_i^0 and the conversion degrees a_i known, the

108 volume fractions of decomposed constituents f_i^d , residual constituents f_i^r , and
109 decomposed water f_i^w can be respectively obtained as follows:

$$110 \quad f_i^d = f_i^0 a_i \quad (1)$$

$$111 \quad f_i^r = f_i^0 (1 - a_i) \quad (2)$$

$$112 \quad f_i^w = f_i^d n_i^w \frac{\rho_i / M_i}{\rho_w / M_w} \quad (3)$$

113 where the subscript i represents different hydration products, w represents water, n_i^w is the
114 amount of water in mole decomposed per mole of reactant i , and ρ and M with
115 subscripts are the mass density and molar mass, respectively [26]. By considering
116 decomposed water as additional pores, the variation of the volume fraction of capillary pores
117 can also be estimated with the heating process.

118 Based on the thermal decomposition analysis, the Young's modulus and intrinsic
119 permeability of heated cement paste can be estimated using the models proposed by Zhao et
120 al. [27,28]. In the prediction of Young's modulus [27], with the residual undecomposed phase
121 and the decomposition products treated as matrix and inclusion, respectively, a two-phase
122 composite sphere model is developed. By analyzing the porosities of decomposition products,
123 the Young's modulus of the inclusion can be estimated according to the granular mechanics.
124 A two-step approach is then adopted to evaluate the Young's modulus of cement paste as a
125 function of heating history.

126 For the prediction of the intrinsic permeability [28], cement paste is represented by three
127 two-phase composite constituents since pores of different scales coexist in cement paste. By
128 applying the effective medium theory, the intrinsic permeability of heated cement paste can
129 be formulated in terms of the volume fractions and permeabilities of various constituents in
130 cement paste. To consider the effect of slip-flow on the intrinsic permeability to gas, the

131 relation proposed by Klinkenberg [29] is adopted. By adopting the expression of Klinkenberg
 132 constant proposed by Chung and Consolazio [30] and accounting for the blocking effect of
 133 liquid water [30], the effective intrinsic permeability to gas can be obtained [31].

134 **2.2. Temperature field**

135 According to the principle of energy conservation and Fourier's law, the transient
 136 temperature field is governed by

$$137 \quad \rho c \dot{T} = \frac{\partial}{\partial x_i} \left(\lambda_{ci} \frac{\partial T}{\partial x_i} \right) + \dot{\phi} \quad (4)$$

138 where ρ , c , λ_{ci} , T , and $\dot{\phi}$ are the mass density, the specific heat, the thermal conductivity,
 139 the temperature, and the internal heat source, respectively. With the parameters known, the
 140 temperature field in the solid body under specified boundary conditions can be determined by
 141 solving the governing equation with the finite element method.

142 **2.3. Vapor pressure and moisture transport**

143 Under high temperature conditions, vapor pressure will build up in concrete and
 144 contribute to the thermo-mechanical damage to concrete. According to thermodynamics, the
 145 vapor phase in concrete can be either saturated vapor or superheated steam. By taking the
 146 volume fraction of dry air and its effect on vapor pressure as negligibly small, for a given
 147 temperature and specific volume of moisture, the vapor pressure can be determined from
 148 steam tables. The specific volume of moisture in capillary pores is given by

$$149 \quad v = \frac{V_m}{m_m} = \frac{f_{cap} \cdot V_0}{f_{cap} \cdot V_0 \rho_w S_d} = \frac{1}{\rho_w S_d} \quad (5)$$

150 where V_m and m_m are the volume and mass of the moisture, respectively, f_{cap} is the
 151 capillary porosity, V_0 is the bulk volume of cement paste, and S_d is the moisture content
 152 defined as

153

$$S_d = \frac{V_l + V_v \cdot \rho_v / \rho_w}{f_{cap} \cdot V_0} \quad (6)$$

154

with V_l and V_v being the volumes of the liquid phase and vapor phase of moisture in the

155

capillary pores, respectively, and ρ_v being the mass density of vapor. The degree of water

156

saturation of capillary pores, which is used in the moisture transport analysis, can also be

157

obtained as

158

$$S_w = \frac{V_l}{f_{cap} \cdot V_0} \quad (7)$$

159

In the determination of vapor pressure, since it is mainly induced by free water in capillary

160

pores [32], only free water in capillary pores is considered and the thermal decomposition

161

effects on the moisture content and the capillary porosity are accounted for. Moreover, as the

162

surface tension of water decreases with the increase of temperature and reaches zero value at

163

the critical point of 374.15 °C, the meniscus effect of the interface between liquid water and

164

water vapor on the vapor pressure, which is governed by the Kelvin equation, is ignored.

165

When concrete is exposed to elevated temperatures, a moisture transport driven by the

166

gradient of build-up vapor pressure occurs. In view of the low permeability of concrete,

167

which results in a low velocity of moisture flow, Darcy's law is used for the description,

168

$$q = -k \nabla p \quad (8)$$

169

where q is the moisture flux, k is the permeability, and p is the pressure. In modeling the

170

mass transport, only the transport in vapor phase is considered since the transport in liquid

171

phase is negligibly small compared with that in vapor phase [30,33]. Based on the mass

172

conservation principle, the governing equation of the moisture transport can be derived as

173

$$\frac{\partial}{\partial x_i} \left(k \frac{\partial p}{\partial x_i} \right) - \frac{\partial \rho_v}{\partial t} + \dot{m}_{dh} = 0 \quad (9)$$

174

where t is time and \dot{m}_{dh} is the moisture source from thermal decomposition. The

175 permeability k is given by

$$176 \quad k = \rho_v \frac{k'_s}{\eta} \quad (10)$$

177 with η being the dynamic viscosity of vapor and k'_s being the effective intrinsic
178 permeability to gas. By applying the Galerkin weighted-residual scheme, the moisture
179 transport is analyzed with the finite element method.

180 **2.4. Poro-mechanical analysis**

181 To account for the effect of vapor pressure on the stress and strain fields in concrete, the
182 poro-elastic theory [34] is applied since concrete can be considered as a porous medium due
183 to the presence of pores in cement paste. Thus, the total strain tensor ε_{ij} is related to the
184 stress tensor σ_{ij} and the vapor pressure p by [35,36]

$$185 \quad \varepsilon_{ij} = \frac{1}{2G} \left[\sigma_{ij} - \frac{\nu}{1+\nu} \sigma_{kk} \delta_{ij} \right] + \frac{1}{3H} p \delta_{ij} + \varepsilon_{th}^e \delta_{ij} \quad (11)$$

186 where G is the drained shear modulus, ν is the drained Poisson's ratio, δ_{ij} is the
187 Kronecker delta, $1/H$ is the Biot modulus, ε_{th}^e is the effective thermal strain. In the
188 derivation of Eq. (11) [36], the transient creep strain [37,38] is decomposed into a material
189 degradation-induced strain and a microcracking-induced thermal strain. The former is
190 reflected in the variation of Young's modulus and the latter is accounted for by deducting it
191 from the free thermal strain and the effective thermal strain ε_{th}^e is then obtained and equal to

$$192 \quad \varepsilon_{th}^e = \alpha_t^e \cdot \Delta T \quad (12)$$

193 with α_t^e and ΔT being the effective thermal expansion coefficient and the temperature
194 change, respectively. According to poro-mechanics [35], the effective stress, which governs
195 the elastic volume change and failure behavior of concrete, is as follows

$$196 \quad \sigma_{ij}^e = \sigma_{ij} + \alpha_b \cdot p \delta_{ij} \quad (13)$$

197 where α_b is the Biot-Willis coefficient, which is taken to be the capillary porosity [31], and
 198 $\alpha_b \cdot p$ is defined as the effective vapor pressure.

199 **2.5. Non-linear mechanical analysis**

200 For the cracking and spalling modeling, the theory of fixed anisotropic smeared crack is
 201 adopted. Prior to cracking, both the aggregate and the cement paste are modeled as
 202 linear-elastic isotropic materials. Once the combination of effective principal stresses reaches
 203 the tension cut-off criterion, a crack perpendicular to the direction of the principal stress is
 204 initiated and its orientation is fixed thereafter. At this stage, the initial isotropic constitutive
 205 relation is replaced by the orthotropic one with fixed axes of orthotropy. The evolution of
 206 cracking damage is considered by degrading the Young's modulus in the cracking direction as

$$207 \quad E_i = \alpha_i E_c \quad (14)$$

208 where E_c is the Young's modulus of undamaged concrete and α_i ($0 \leq \alpha_i \leq 1$) are the
 209 damage variables, which reflect the degrading degrees of E_i . To describe the cracking
 210 damage evolution in the local n - s coordinate system, the loading function is as follows

$$211 \quad f(\varepsilon'_{nn}, \kappa) = \varepsilon'_{nn} - \kappa \quad (15)$$

212 where κ is a history-dependent damage parameter used for memorizing the highest value of
 213 ε'_{nn} , which is defined as

$$214 \quad \varepsilon'_{nn} = \varepsilon_{nn} - \varepsilon_{th}^e \quad (16)$$

215 The loading function of Eq. (15) is subjected to the standard Kuhn-Tucker loading-unloading
 216 conditions [39]

$$217 \quad f \leq 0, \quad \dot{\kappa} \geq 0, \quad f \cdot \dot{\kappa} = 0 \quad (17)$$

218 where $\dot{\kappa}$ is the rate of κ . During the whole loading process, the value of κ increases
 219 monotonically. The evolution of damage variable α in Eq. (14) is inferred from the tensile
 220 stress-strain relation shown in Fig. 1 and expressed as a function of κ as

221
$$\alpha = \alpha(\kappa) = \begin{cases} 1, & \text{if } \kappa \leq \varepsilon_e \\ (\varepsilon_e / \kappa) \exp[-\mu(\kappa - \varepsilon_e)], & \text{if } \kappa > \varepsilon_e \end{cases} \quad (18)$$

222 where ε_e is the strain at the peak stress under uniaxial tension, and μ is a parameter that
 223 controls the slope of the exponential strain softening curve and can be determined from the
 224 fracture energy. Since the fixed anisotropic smeared cracking model is adopted, to reflect the
 225 capacity of a crack to transfer shear stress in mode-II fracture, a shear retention factor is used
 226 and taken as inversely proportional to the crack strain ε_{cr} [39], which is given by [36]

227
$$\varepsilon_{cr} = (1 - \alpha) \varepsilon'_m \quad (19)$$

228 Since the magnitudes and directions of the stress and strain in heated concrete may change
 229 with temperature field evolution, a stiffness recovery caused by crack closure is also
 230 considered in the analysis.

231 For the non-linear mechanical analysis, the Newton-Raphson iteration method is used in
 232 conjunction with the finite element method based on the principle of minimum potential
 233 energy. Since HPC is rather brittle and spalling usually occurs without warning, it is
 234 reasonable to ignore the geometrical non-linear effect in the spalling modeling. Thus, when
 235 the non-linear iteration fails to converge, which means that concrete can no longer sustain the
 236 thermo-mechanical loading, spalling occurs. From the cracking pattern and the stress
 237 distribution before failure, the manner of spalling can be deduced. To evaluate the energy
 238 stored in heated concrete, the elastic strain energy for two-dimensional analysis can be
 239 calculated as follows

240
$$I_c = \sum_{k=1}^{ne} \frac{1}{2} \sigma_{ij}^e \varepsilon'_{ij} A_e \quad (20)$$

241 where σ_{ij}^e is the effective stress, ε'_{ij} is the elastic strain, A_e is the surface area of each
 242 element, and ne is the number of elements.

243

244 3. Heating rate effect on spalling

245 To analyze the heating rate effect on spalling of HPC, the thermo-mechanical behavior of
246 100 mm cubic HPC specimens with an initial moisture content of 90% exposed to the ISO
247 834 standard fire (Fig. 2) and a slow heating with a heating rate of 5 °C/min reported in
248 Peng's test [4] is numerically modeled at a meso-level. In Peng's test [4], ordinary Portland
249 cement (OPC 52.5) with a chemical composition of C₃S-55.8%, C₂S-15.8%, C₃A-9.2%, and
250 C₄AF-9.1% by mass was used. Ten percent cement by mass was replaced by silica fume.
251 Crushed granite and river sand with a density of 2.62 g/cm³ were used as coarse and fine
252 aggregates, respectively. The volume content of aggregate was 64.8%. The water to binder
253 ratio was 0.26. The spalling test was conducted at a curing age of 90 days. The measured
254 compressive strength, tensile strength, and Young's modulus of concrete at room temperature
255 were 115 MPa, 7.2 MPa, and 42 GPa, respectively. During the test, the temperature evolution
256 in the specimens was recorded. It has been found that, under fire exposure, explosive spalling
257 occurred when the surface temperatures of the specimens were in the range of 480 to 510 °C.
258 However, under slow heating, the specimens did not spall. Since the probability of explosive
259 spalling was not 100%, the un-spalled specimens exposed to fire and the specimens exposed
260 to slow heating were sawn in half for the observation of internal cracks as shown in Fig. 3.

261 In the numerical modeling, a two-dimensional analysis is conducted at a meso-level as
262 shown in Fig. 4. The concrete cube is modeled as a two-phase composite consisting of
263 aggregates and cement paste in view of the fact that the interfacial transition zone (ITZ) effect
264 is negligibly small for HPC [4]. The aggregates are treated as spheres and randomly
265 distributed according to the aggregate gradation reported in the experiments [4,40] as shown
266 in Fig. 4b. Three-node triangle elements are used for the discretization.

267 The thermal material properties used in the temperature analysis are listed in Table 1.
268 The mass densities are obtained from the experiment [4] and the other values in Table 1 are

269 obtained from the inverse analysis according to the measured temperature evolutions at the
270 four measuring points shown in Figs. 4 and 5. For the thermal decomposition analysis, the
271 hydration degree of cement and silica fume are estimated to be 55% and 50%, respectively,
272 according to the prediction model proposed by Parrot and Killoh [41] and the experimental
273 investigation of Lu et al. [42]. Thus, from the chemical composition of the used cement [4],
274 the original volume fractions of various constituents in cement paste are obtained as shown in
275 Table 2 with the method proposed by Zhao et al. [26]. Based on the thermal decomposition
276 analysis, the Young's modulus and intrinsic permeability of cement paste can then be
277 predicted with the proposed models [27, 28] according to the temperature distribution
278 evolution. The Young's modulus of granite aggregate at room temperature is taken as 45 GPa
279 [43] and, at high temperatures, its relative value first gradually decreases from 1 at 20 °C to
280 0.967 at 200 °C, then continues to decrease up to 0.77 at 400 °C, and afterwards keeps
281 constant [44]. For the permeability of aggregate, it has been reported that the permeability of
282 granite is very low, that is, at room temperature, the permeability is in the range of 5×10^{-20} to
283 $1 \times 10^{-19} \text{ m}^2$ [45-47] and, at high temperatures, the permeability decreases with the increase in
284 temperature [45, 46]. Thus, the aggregate is considered impermeable in the analysis. The
285 effective expansion coefficient is taken as $1.5 \times 10^{-6} \text{ }^\circ\text{C}^{-1}$ for both cement paste and aggregate
286 [36]. Although it will be more precise if the strength and constitutive law of individual
287 component are considered in the meso-level analysis, owing to the lack of experimental data,
288 the strengths and constitutive laws of cement paste and aggregate at room temperature are
289 approximately taken to be those of concrete. At high temperatures, the decrease in the
290 strength of materials is correlated with the degradation in the Young's modulus according to
291 the descending branch of the constitutive relation shown in Fig. 1. From the measured
292 fracture energy of 165 N/m, the strain softening parameter is estimated to be 2686 with the
293 crack band model proposed by Bažant [48].

294 With these inputs and time intervals of 5 seconds and 2 minutes for fire heating and slow
295 heating, respectively, the thermo-chemo-hydro-mechanical analyses are conducted by
296 applying the same boundary conditions as in the experiment. The temperature evolutions and
297 temperature distributions at 300 °C surface temperature of the specimens under fire heating
298 and slow heating are shown in Figs. 6 and 7, respectively. It can be seen from these figures
299 that the temperature gradient under fire heating is much greater than that under slow heating.
300 The predicted distributions of effective vapor pressure in the specimens at 400 °C and 500 °C
301 surface temperatures under the two heating conditions are shown in Figs. 8 and 9,
302 respectively. It can be seen from these figures that the vapor pressure distributions under the
303 two heating conditions are quite different. Under fire heating, the vapor pressure resides in
304 the outer layer of the specimen and the peak moves inwardly with the evolution of
305 temperature, while, under slow heating, high vapor pressure evenly distributes in the central
306 region owing to the low temperature gradient.

307 To investigate the effects of the temperature gradient and vapor pressure on the
308 mechanical behavior of specimens under the two heating conditions, the evolutions of the
309 stress distributions induced only by vapor pressure and only by temperature gradient are
310 shown in Figs. 10 to 13, respectively. Since the temperature gradient in the specimen under
311 slow heating does not change much (Fig. 6b), the stress distribution shown in Fig. 13 keeps
312 nearly stable for the whole heating process. It can be seen from Fig. 12 that the tensile
313 thermal stress induced by the temperature gradient under fire heating evolves from the
314 corners to the central region of the specimen and its magnitude is much higher than that under
315 slow heating as shown in Fig. 13. By comparing Figs. 10 and 11 with Figs. 8 and 9, it can be
316 seen that the vapor pressure induced stress associates with the vapor pressure distribution, i.e.
317 the stress exists where the vapor pressure exists. Thus, vapor pressure has a local effect on the
318 induced stress.

319 When the effects of the temperature gradient and vapor pressure are both taken into
320 account, for fire heating, the non-linear mechanical analysis fails to converge when the
321 surface temperature of the specimen reaches 476.1 °C, which means spalling occurs. For slow
322 heating, however, despite some damaged elements in the matrix, no divergence occurs for the
323 whole heating process, which implies no spalling occurs. It is in agreement with the
324 experimental results. The damage patterns and effective first principal stresses of the
325 specimens under fire heating just before spalling and under slow heating at 600 °C are shown
326 in Figs. 14 and 15, respectively. The evolutions of the elastic strain energy under the two
327 heating conditions are shown in Fig. 16, where the total strain energy is subdivided into the
328 strain energy induced by the temperature gradient and the strain energy increment induced by
329 vapor pressure.

330 For fire heating, it can be inferred from Fig. 14 that the spalling mode of HPC is
331 explosive since the effective first principal stress in the central region is the highest and some
332 cracks exist in the central region already. Comparing Fig. 14a with Fig. 3a, it can be seen that
333 the predicted cracking pattern is similar to the experimentally observed one. Therefore, the
334 numerical result of fire spalling correlates well with the experimental results in terms of both
335 the spalling time and the damage pattern. By comparing Fig. 14b with Figs. 10 and 12, it can
336 be concluded that fire spalling is mainly caused by the temperature gradient induced thermal
337 stress since the thermal stress induced by temperature gradient in the central region is much
338 higher than that induced by vapor pressure. The conclusion can also be confirmed by the
339 energy analysis. It can be seen from Fig. 16a that, at the time of spalling, the energy induced
340 by the temperature gradient reaches the highest value and the energy increment induced by
341 vapor pressure counts only 11.2% the total strain energy. For slow heating, however, it can be
342 concluded that the damage shown in Fig. 15a is mainly caused by the build-up vapor pressure
343 since the temperature gradient induced stress and strain energy are much lower than those

344 induced by vapor pressure as shown in Figs. 11, 13 and 16b. Thus, it can be inferred from the
345 analysis that at different heating rates, the spalling mechanisms can be different.

346

347 **4. Discussions**

348 Although the material properties, size, and shape of concrete specimens can also exert
349 tremendous effects on the occurrence of spalling, which is out of the scope of this paper,
350 some interpretations of spalling can still be drawn from the analysis as follows:

351 First, under fast heating conditions, in addition to the explosive spalling as in this study,
352 the probable spalling manner of cubic specimens can also be corner spalling as encountered
353 in the experiment of Yan et al [6]. It can be seen from Fig. 12 that the temperature gradient
354 induced tensile thermal stress evolves from the corners of the specimen and together with the
355 vapor pressure induced stress as shown in Fig. 10, corner spalling can be induced.

356 Second, under fast heating conditions, surface spalling of concrete can occur as reported
357 in the experiments of Yan et al. [5], Yan et al [6], and Klingsch et al. [8]. From the vapor
358 pressure induced stress distribution shown in Fig. 10 it can be seen that surface spalling is
359 possible since vapor pressure evolves from the surface layer of concrete and together with the
360 compressive stress induced by the temperature gradient, surface spalling can occur.

361 Third, under slow heating conditions, concrete specimens can spall into small pieces as
362 shown in the experiments of Yan et al [6] and Debicki et al. [49]. This is because the vapor
363 pressure distributes much evenly and hence induces evenly distributed tensile stress and
364 damage in the matrix as shown in Figs. 11 and 15. Thus, it is possible that concrete spalls into
365 small pieces.

366 Forth, under fire exposure, the spalling mechanism can evolve from temperature gradient
367 governed spalling to vapor pressure governed spalling. Due to the fast decrease in the heating
368 rate as shown in Fig. 2b, the temperature gradient in concrete decreases with the heating

369 process and hence the induced thermal stress effect on spalling decreases. The trend can also
370 be seen from the energy development in the case of this study as shown Fig. 16a, where the
371 temperature gradient induced strain energy decreases after reaching the peak at around 470 °C.
372 On the other hand, with the decrease in the temperature gradient, the vapor pressure effect
373 penetrates from the surface to the interior of concrete and becomes more evenly distributed as
374 shown in Figs. 8 and 10. Thus, if concrete can sustain the temperature gradient induced
375 thermal stress in the early stage of fire heating, the vapor pressure effect will take the lead in
376 spalling.

377

378 **5. Conclusions**

379 The heating rate effect on spalling of 100 mm cubic HPC specimens has been
380 numerically investigated based on the experiments reported in the literature. In the analysis,
381 the effects of two heating conditions, i.e. ISO 834 standard fire and slow heating with a
382 heating rate of 5 °C/min, on the thermal mechanical behavior of HPC cubes have been
383 compared and studied at a meso-level. By conducting the thermo-chemo-hydro-mechanical
384 analysis, the effects of the temperature-gradient and vapor pressure on the stress distribution
385 and damage pattern have been numerically quantified. It can be concluded that **the spalling**
386 **mechanisms of HPC are different under different heating conditions:** for fire heating, the
387 temperature-gradient induced thermal stress plays a dominant role in spalling of the cube and,
388 for slow heating, the vapor pressure governs the mechanical behavior of the specimen. **It can**
389 **also be inferred from the investigation that, if concrete can sustain the thermal stress at the**
390 **early stage of fire heating, vapor pressure will become the driving force of spalling at the**
391 **later stage of fire because of the decrease in the heating rate. Other spalling manners, such as**
392 **corner spalling, surface spalling, and small pieces spalling, are also discussed and explained**
393 **based on the analysis.**

394

395 **Acknowledgements**

396 The financial support from the National Natural Science Foundation with Grant Nos.
397 51379188 and 51278048 of the People's Republic of China is greatly acknowledged.

398

399 **References**

400 [1] Hertz KD. Danish investigations on silica fume concretes at elevated temperatures. *ACI*
401 *Mater J* 1992; 89 (4): 345–7.

402 [2] Anderberg Y. Spalling phenomena of HPC and OC. In: *Proc. of Int. Workshop on Fire*
403 *Performance of High-Strength Concrete*, NIST. Gaithersburg, MD; 1997. p. 69–73.

404 [3] Phan LT, Carino NJ. Effects of test conditions and mixture proportions on behavior of
405 high-strength concrete exposed to high temperatures. *ACI Mater J* 2002; 99 (1): 54–66.

406 [4] Peng GF. Evaluation of fire damage to high performance concrete, PhD thesis. China:
407 Hong Kong Polytechnic University; 2000.

408 [5] Yan ZG, Shen Y, Zhu HH, Li XJ, Lu Y. Experimental investigation of reinforced concrete
409 and hybrid fibre reinforced concrete shield tunnel segments subjected to elevated
410 temperature. *Fire Saf J* 2015; 71: 86–99.

411 [6] Yan X, Li H, Wong YL. Effect of aggregate on high-strength concrete in fire. *Mag Concr*
412 *Res* 2007; 59 (5): 323–8.

413 [7] Kanéma M, Pliya P, Noumowé A, Gallias JL. Spalling, thermal, and hydrous behavior of
414 ordinary and high-strength concrete subjected to elevated temperature. *J Mater Civil Eng*
415 2011; 23 (7): 921–30.

416 [8] Klingsch EW, Frangi A, Fontana M. High- and ultra-high-performance concrete: a
417 systematic experimental analysis on spalling. *ACI Special Publication* 2011; 279: 1–50.

418 [9] Ulm FJ, Coussy O, Bažant ZP. The 'Chunnel' fire I: chemoplastic softening in rapidly

- 419 heated concrete. *J Eng Mech* 1999; 125 (3): 272–82.
- 420 [10] Ulm FJ, Acker P, Lévy M. The ‘Chunnel’ fire II: analysis of concrete damage. *J Eng*
421 *Mech* 1999; 125 (3): 283–9.
- 422 [11] Ichikawa Y, England GL. Prediction of moisture migration and pore pressure build-up in
423 concrete at high temperatures. *Nucl Eng Des* 2004; 228 (1–3): 245–59.
- 424 [12] Dwaikat MB, Kodur VKR. Hydrothermal model for predicting fire-induced spalling in
425 concrete structural systems. *Fire Saf J* 2009; 44 (3): 425–34.
- 426 [13] Beneš M, Štefan R. Hygro-thermo-mechanical analysis of spalling in concrete walls at
427 high temperatures as a moving boundary problem. *Int J Heat Mass Transfer* 2015; 85:
428 110–34.
- 429 [14] Tenchev R, Purnell P. An application of a damage constitutive model to concrete at high
430 temperature and prediction of spalling. *Int J Solids Struct* 2005; 42 (26): 6550–65.
- 431 [15] Gawin D, Pesavento F, Schrefler BA. Towards prediction of the thermal spalling risk
432 through a multi-phase porous media model of concrete. *Comput Meth Appl Mech Eng*
433 2006; 195 (41–43): 5707–29.
- 434 [16] De Moraes MVG, Pliya P, Noumowé A, Beaucour AL, Ortola S. Contribution to the
435 explanation of the spalling of small specimen without any mechanical restraint exposed
436 to high temperature. *Nucl Eng Des* 2010; 240 (10): 2655–63.
- 437 [17] Fu YF, Li LC. Study on mechanism of thermal spalling in concrete exposed to elevated
438 temperatures. *Mater Struct* 2011; 44: 361–76.
- 439 [18] Zhang HL, Davie CT. A numerical investigation of the influence of pore pressures and
440 thermally induced stresses for spalling of concrete exposed to elevated temperatures. *Fire*
441 *Saf J* 2013; 59: 102–10.
- 442 [19] Zhang YM, Zeiml M, Pichler C, Lackner R. Model-based risk assessment of concrete
443 spalling in tunnel linings under fire loading. *Eng Struct* 2014; 77: 207–15.

- 444 [20] Xotta G, Mazzucco G, Salomoni VA, Majorana CE, Willam KJ. Composite behavior of
445 concrete materials under high temperatures. *Int J Solids Struct* 2015; 64–65: 86–99.
- 446 [21] Ju Y, Liu JH, Liu HB, Tian KP, Ge ZS. On the thermal spalling mechanism of reactive
447 powder concrete exposed to high temperature: Numerical and experimental studies. *Int J*
448 *Heat Mass Transfer* 2016; 98: 493–507.
- 449 [22] Sanjayan G, Stocks LJ. Spalling of high-strength silica fume concrete in fire. *ACI Mater*
450 *J* 1993; 90 (2): 170–3.
- 451 [23] Bažant ZP. Analysis of pore pressure, thermal stress and fracture in rapidly heated
452 concrete. In: *NIST Int. Workshop on Fire Performance of High-Strength Concrete*.
453 Gaithersburg, MD, USA; 1997. p. 155–64.
- 454 [24] Dougill JW. Modes of failure of concrete panels exposed to high temperatures. *Mag*
455 *Concr Res* 1972; 24 (79): 71–6.
- 456 [25] Jansson R. Material properties related to fire spalling of concrete, PhD thesis. Sweden:
457 Lund Institute of Technology; 2008.
- 458 [26] Zhao J, Zheng JJ, Peng GF, van Breugel K. Prediction of thermal decomposition of
459 hardened cement paste. *J Mater Civil Eng* 2012; 24 (5): 592–8.
- 460 [27] Zhao J, Zheng JJ, Peng GF. A numerical method for predicting Young's modulus of
461 heated cement paste. *Constr Build Mater* 2014; 54: 197–201.
- 462 [28] Zhao J, Zheng JJ, Peng GF. An effective medium approach for predicting the intrinsic
463 permeability of heated cement paste. *Adv Cem Res* 2015; 27 (4): 240–6.
- 464 [29] Klinkenberg LJ. The permeability of porous media to liquids and gases. *Drilling and*
465 *Production Practice*. American Petroleum Institute, Washington DC, USA; 1941. p.
466 200–13.
- 467 [30] Chung JH, Consolazio GR. Numerical modeling of transport phenomena in reinforced
468 concrete exposed to elevated temperatures. *Cem Concr Res* 2005; 35 (3): 597–608.

- 469 [31] Zhao J. Fire-induced spalling modeling of high-performance concrete, PhD thesis. The
470 Netherlands: Delft University of Technology; 2012.
- 471 [32] Mindeguia JC, Pimienta P, Hager I, Carré H. Influence of water content on gas pore
472 pressure in concretes at high temperature. In: 2nd Int. RILEM Workshop on Concrete
473 Spalling due to Fire Exposure. Delft, the Netherlands; 2011. p.113–21.
- 474 [33] Gawin D, Pesavento F, Schrefler BA. Modelling of hygro-thermal behaviour of concrete
475 at high temperature with thermo-chemical and mechanical material degradation. *Comput
476 Meth Appl Mech Eng* 2003; 192 (13–14): 1731–71.
- 477 [34] Biot MA. General theory of three-dimensional consolidation. *J Appl Phys* 1941; 12:
478 155–64.
- 479 [35] Coussy O. *Poromechanics*. England: John Wiley & Sons Ltd; 2004.
- 480 [36] Zhao J, Zheng JJ, Peng GF, van Breugel K. A meso-level investigation into the explosive
481 spalling mechanism of high-performance concrete under fire exposure. *Cem Concr Res*
482 2014; 65: 64–75.
- 483 [37] Anderberg Y, Thelandersson S. Stress and deformation characteristics of concrete-2.
484 experimental investigation and material behaviour model. Bulletin 54, Lund institute of
485 technology, Sweden; 1976.
- 486 [38] Khoury GA, Grainger BN, Sullivan PJE. Strain of concrete during first heating to 600 °C
487 under load. *Mag Concr Res* 1985; 37 (133): 195–215.
- 488 [39] Rots JG. Computational modeling of concrete fracture, PhD thesis. The Netherlands:
489 Delft University of Technology; 1988.
- 490 [40] Zheng JJ, Li CQ, Zhao LY. Simulation of two-dimensional aggregate distribution with
491 wall effect. *J Mater Civil Eng* 2003; 15 (6): 506–10.
- 492 [41] Parrot LJ, Killoh DC. Prediction of cement hydration. *Br Ceram Proc* 1984; 35: 41–53.
- 493 [42] Lu P, Sun Gk, Young JF. Phase composition of hydrated DSP cement pastes. *J Am*

494 Ceram Soc 1993; 76 (4): 1003–7.

495 [43] Bažant ZP, Kaplan MF. Concrete at high temperatures: material properties and
496 mathematical models. England: Longman Group Ltd; 1996.

497 [44] Wan ZJ, Zhao YS, Dong FK, Feng ZJ, Zhang N, Wu JW. Experimental study on
498 mechanical characteristics of granite under high temperatures and triaxial stresses. Chin J
499 Rock Mech Eng 2008; 27 (1): 72–7. (in Chinese)

500 [45] Morrow C, Lockner D, Moore D, Byerlee J. Permeability of granite in a temperature
501 gradient. J Geophys Res 1981; 86 (B4): 3002–8.

502 [46] Moore DE, Lockner DA, Byerlee JD. Reduction of permeability in granite at elevated
503 temperatures. Science 1994; 265 (5178): 1558–61.

504 [47] Selvadurai APS, Boulon MJ, Nguyen TS. The permeability of an intact granite. Pure
505 Appl Geophys 2005; 162: 373–407.

506 [48] Bažant ZP. Mechanics of distributed cracking, Appl Mech Rev 1986; 39 (5): 675–705.

507 [49] Debicki G, Haniche R, Delhomme F. An experimental method for assessing the spalling
508 sensitivity of concrete mixture submitted to high temperature. Cem Concr Compos 2012;
509 34: 958–63.

510

511

512 **List of figure and table captions:**

513 Fig. 1. Damage variable and exponential stress-strain relation.

514 Fig. 2. (a) Heating curve and (b) heating rate of ISO 834 standard fire.

515 Fig. 3. Internal cracking observation of un-spalled specimen exposed to fire heating and
516 specimen exposed to slow heating [4].

517 Fig. 4. 2D domain of numerical analysis and temperature measuring points.

518 Fig. 5. Comparison of temperature evolution at four measuring points.

519 Fig. 6. Predicted evolution of temperature profile in middle of specimen.

520 Fig. 7. Temperature field at 300 °C surface temperature.

521 Fig. 8. Distribution of effective vapor pressure (MPa) in specimen at (a) 400 °C and (b) 500
522 °C under fire heating.

523 Fig. 9. Distribution of effective vapor pressure (MPa) in specimen at (a) 400 °C and (b) 500
524 °C under slow heating.

525 Fig. 10. Effective first principal stress (Pa) induced by vapor pressure at (a) 400 °C and (b)
526 500 °C under fire heating.

527 Fig. 11. Effective first principal stress (Pa) induced by vapor pressure at (a) 400 °C and (b)
528 500 °C under slow heating.

529 Fig. 12. Evolution of first principal stress (Pa) induced by temperature gradient under fire
530 heating.

531 Fig. 13. First principal stress (Pa) induced by temperature gradient under slow heating.

532 Fig. 14. (a) Damage pattern and (b) effective first principal stress (Pa) just before spalling
533 under fire heating.

534 Fig. 15. (a) Damage pattern and (b) effective first principal stress (Pa) at 600 °C under slow
535 heating.

536 Fig. 16. Evolution of elastic strain energy in specimens under (a) fire heating and (b) slow

537 heating.

538 Table 1. Thermal material properties of aggregate and cement paste.

539 Table 2. Predicted initial volume fractions of various constituents in cement paste.

540

541

Table 1. Thermal material properties of aggregate and cement paste.

Material	Thermal conductivity (W/m·°C)	Specific heat (J/kg·°C)	Mass density (kg/m ³)
Aggregate	5.0	710.0	2620.0
Cement paste	4.0	1175.0	2078.0

Table 2. Predicted initial volume fractions of various constituents in cement paste.

Constituent	Hydrated aluminates	CH	C-S-H	Pozzolanic C-S-H	Unhydrated silica fume	Unhydrated cement	Capillary pore
Volume fraction (%)	8.50	5.37	37.66	14.43	3.82	21.83	8.34

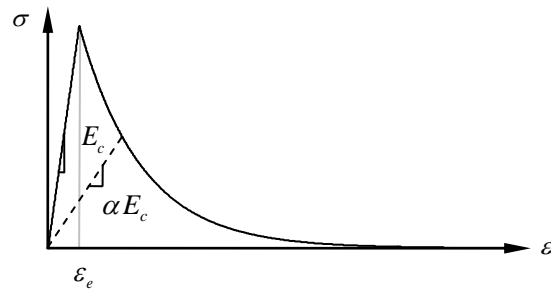
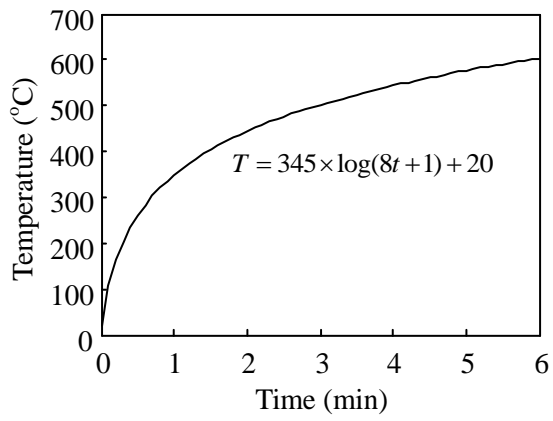
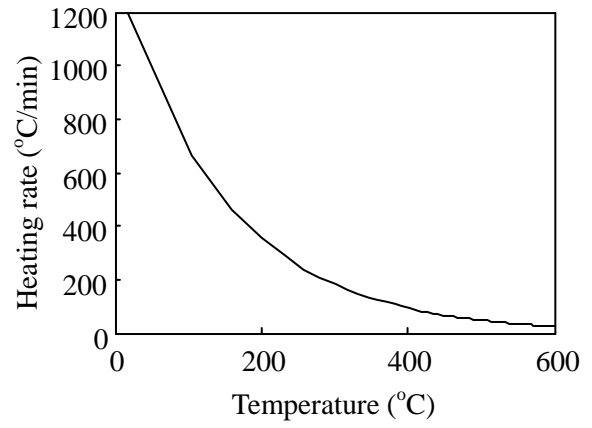


Fig. 1. Damage variable and exponential stress-strain relation.

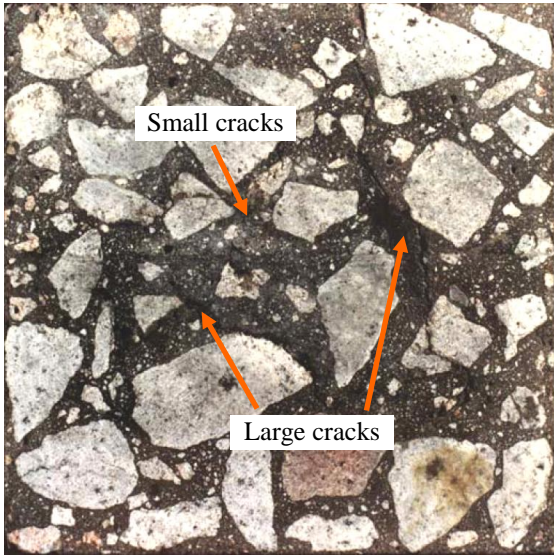


(a)

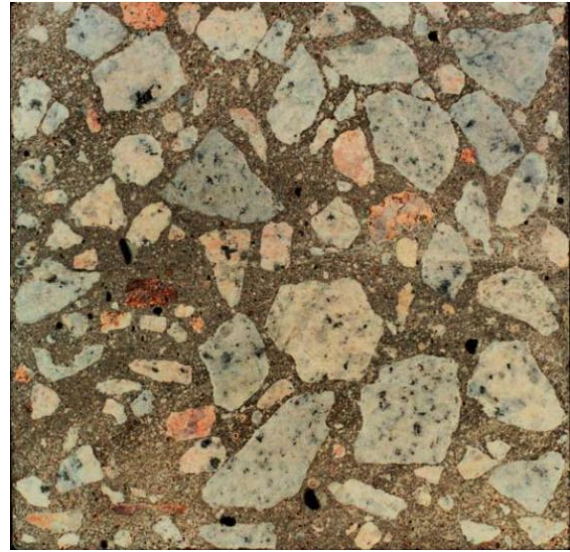


(b)

Fig. 2. (a) Heating curve and (b) heating rate of ISO 834 standard fire.

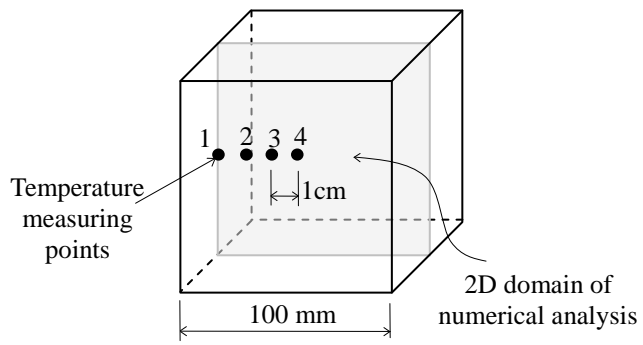


(a)

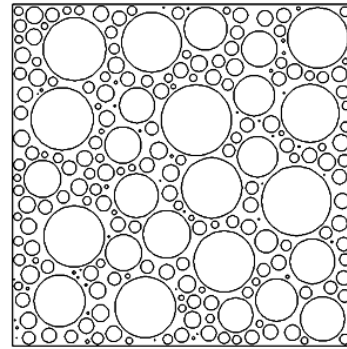


(b)

Fig. 3. Internal cracking observation of un-spalled specimen exposed to fire heating and specimen exposed to slow heating [4].



(a) Concrete cube



(b) Particle distribution of 2D domain

Fig. 4. 2D domain of numerical analysis and temperature measuring points.

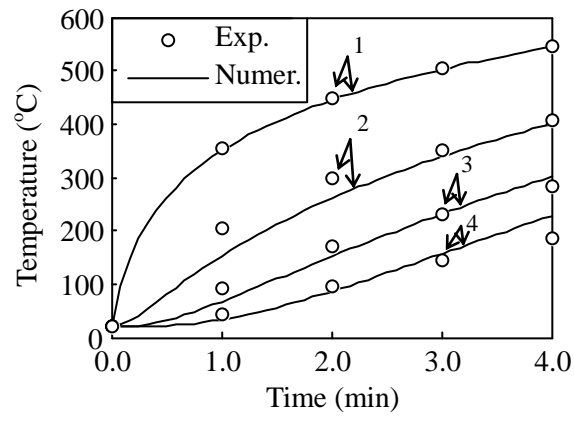
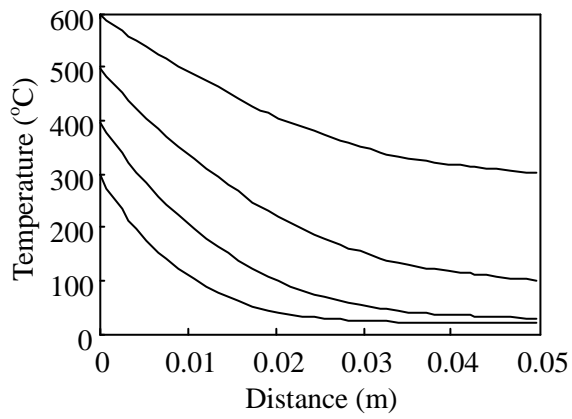
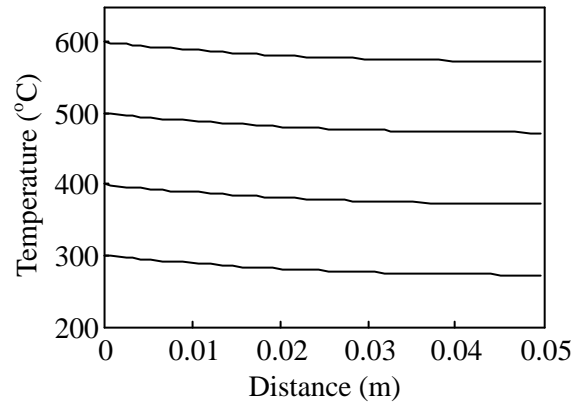


Fig. 5. Comparison of temperature evolution at four measuring points.

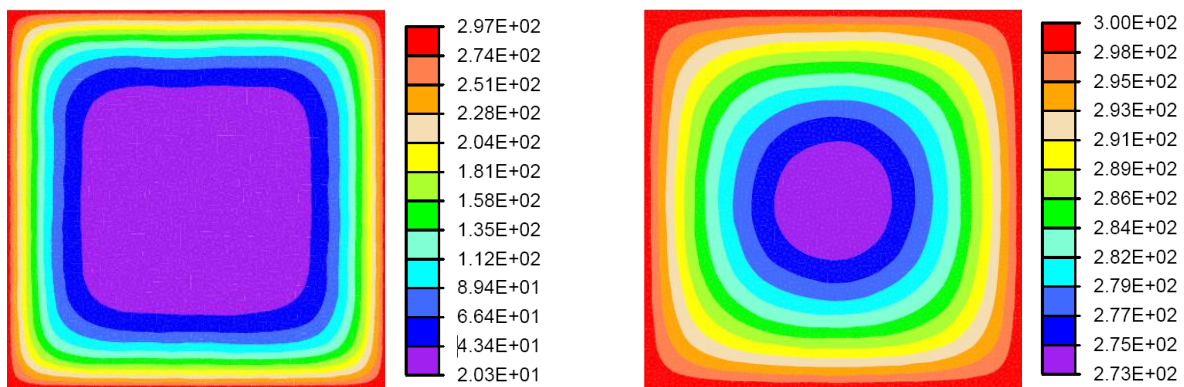


(a) Fire heating



(b) Slow heating

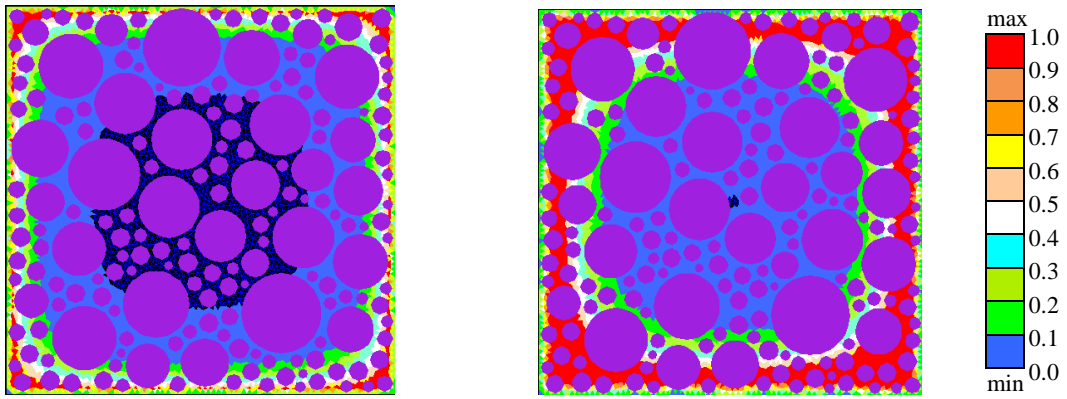
Fig. 6. Predicted evolution of temperature profile in middle of specimen.



(a) Fire heating

(b) Slow heating

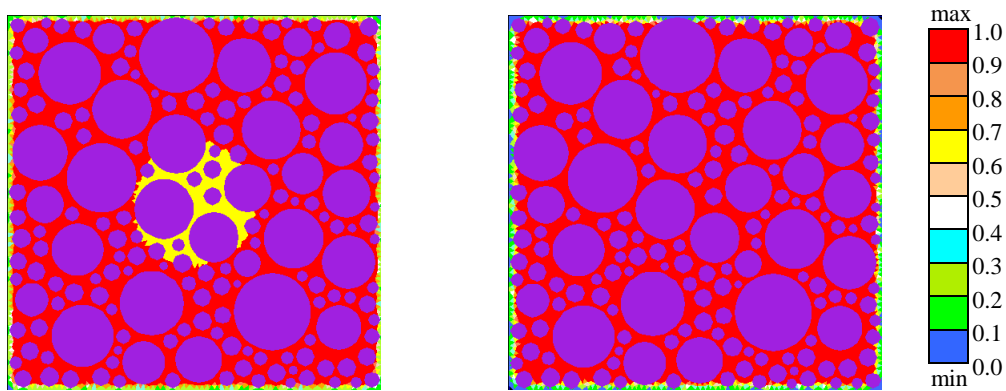
Fig. 7. Temperature field at 300 °C surface temperature.



(a) min=0.00011, max=4.45

(b) min=0.00125, max=4.60

Fig. 8. Distribution of effective vapor pressure (MPa) in specimen at (a) 400 °C and (b) 500 °C under fire heating.



(a) min=0.00010, max=4.45

(b) min=0.00016, max=5.46

Fig. 9. Distribution of effective vapor pressure (MPa) in specimen at (a) 400 °C and (b) 500 °C under slow heating.

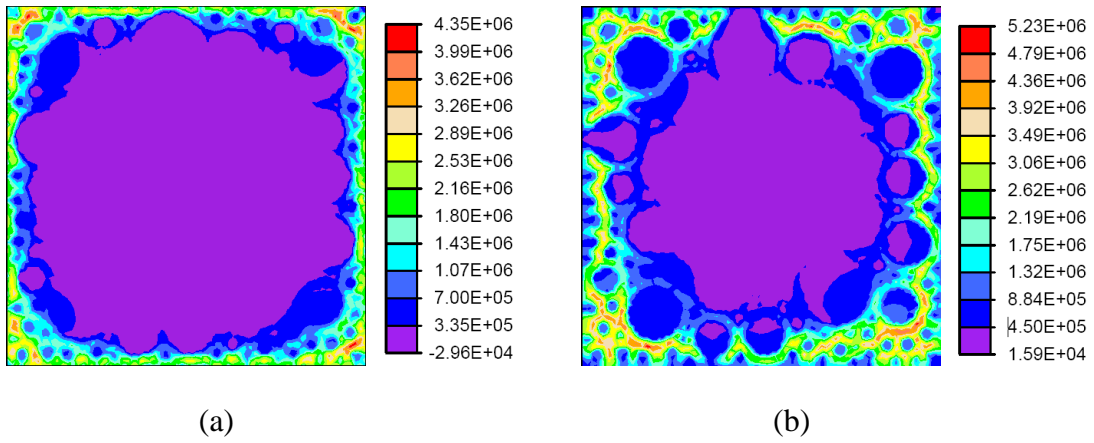


Fig. 10. Effective first principal stress (Pa) induced by vapor pressure at (a) 400 °C and (b) 500 °C under fire heating.

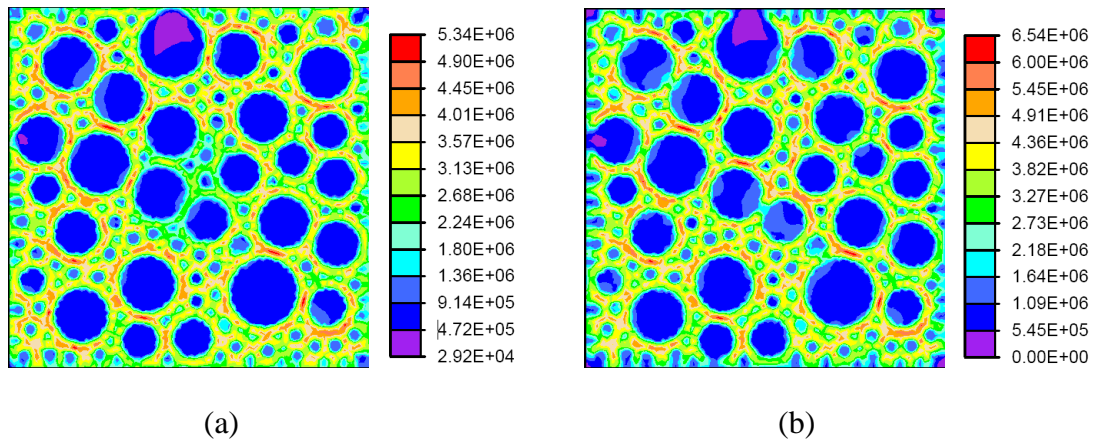


Fig. 11. Effective first principal stress (Pa) induced by vapor pressure at (a) 400 °C and (b) 500 °C under slow heating.

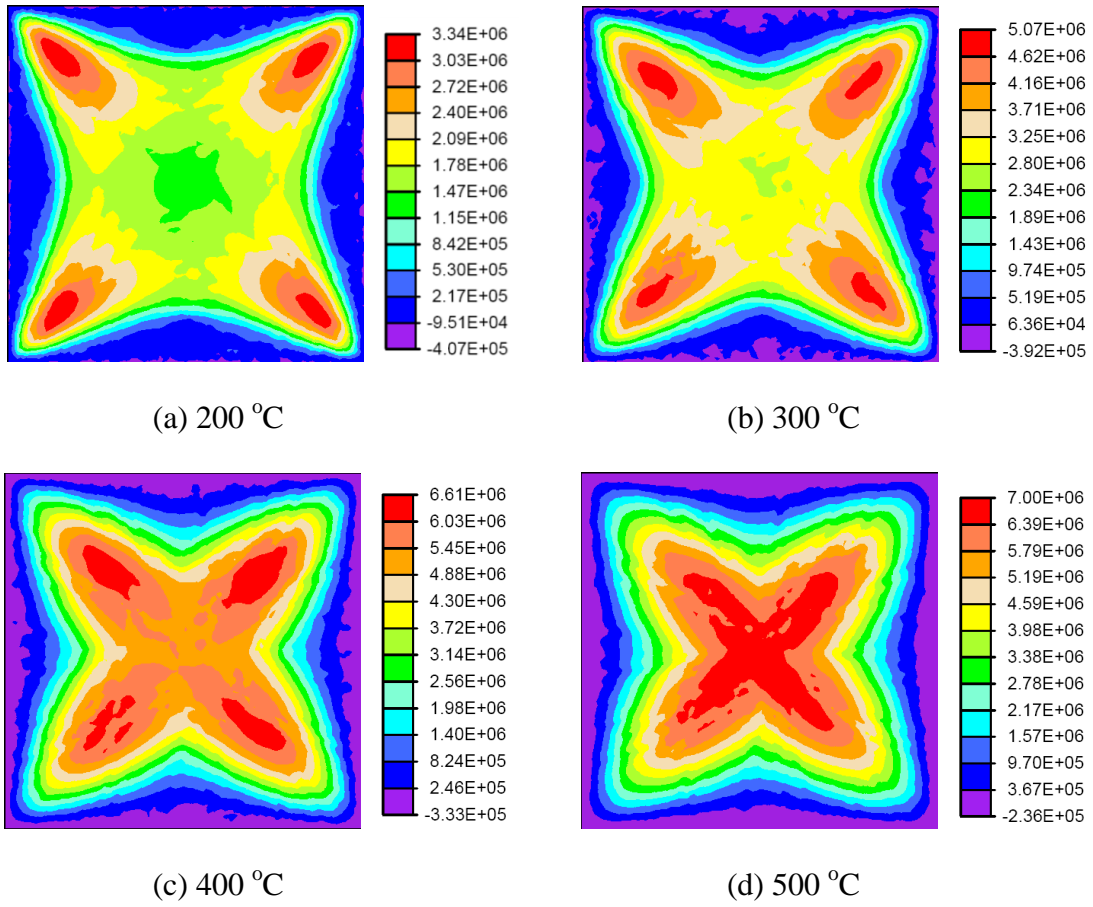


Fig. 12. Evolution of first principal stress (Pa) induced by temperature gradient under fire heating.

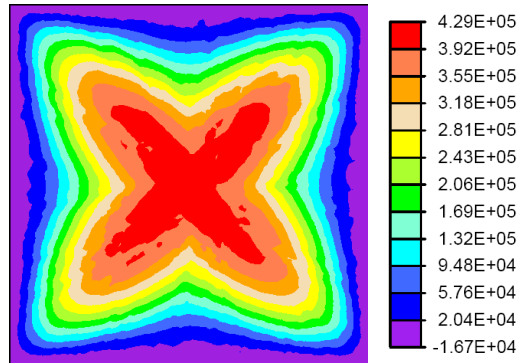


Fig. 13. First principal stress (Pa) induced by temperature gradient under slow heating.

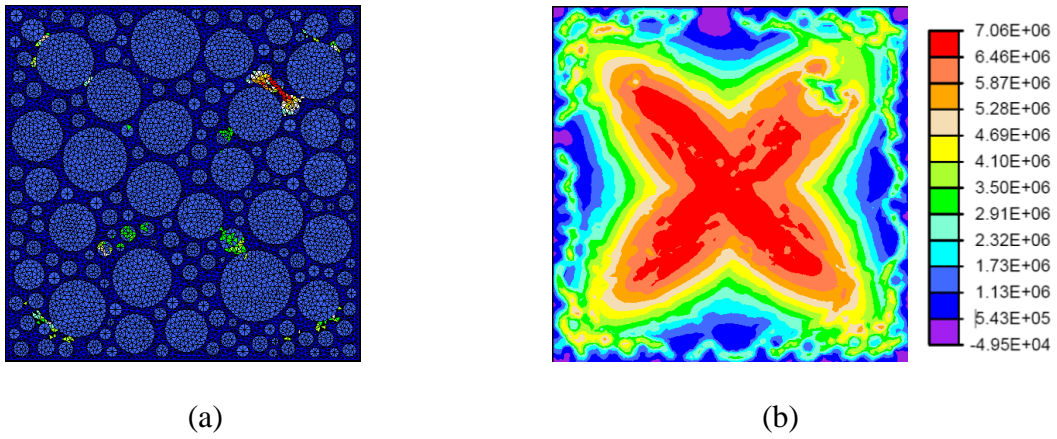


Fig. 14. (a) Damage pattern and (b) effective first principal stress (Pa) just before spalling under fire heating.

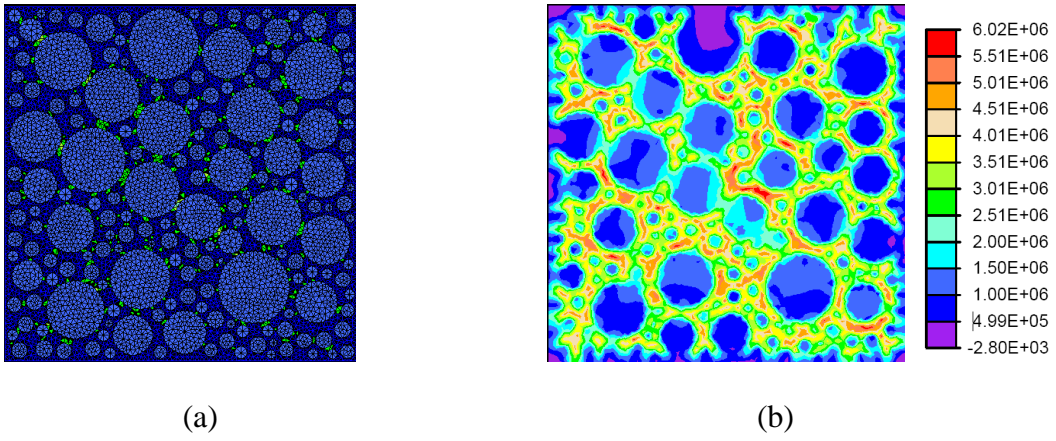
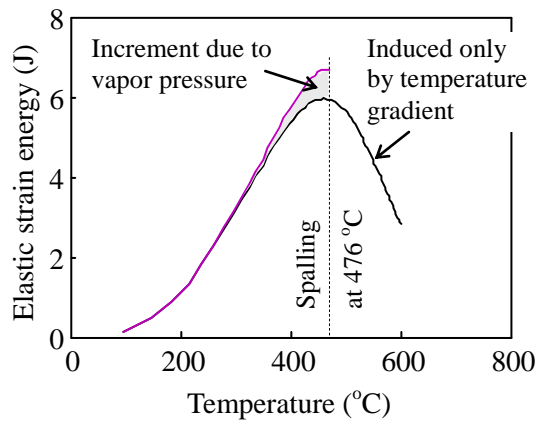
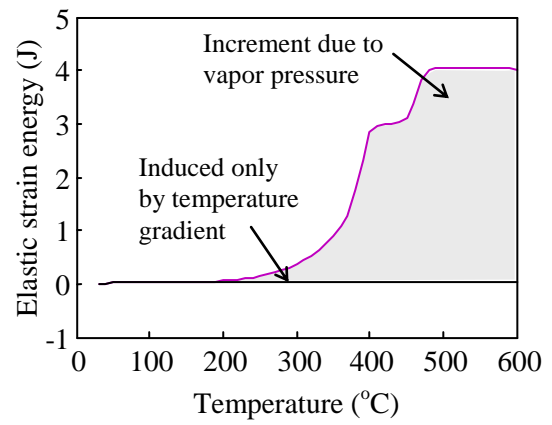


Fig. 15. (a) Damage pattern and (b) effective first principal stress (Pa) at 600 °C under slow heating.



(a)



(b)

Fig. 16. Evolution of elastic strain energy in specimens under (a) fire heating and (b) slow heating.